

Turbulent structures of shock-wave diffraction over 90° convex corner

Cite as: Phys. Fluids 31, 086103 (2019); <https://doi.org/10.1063/1.5113976>

Submitted: 10 June 2019 . Accepted: 11 July 2019 . Published Online: 12 August 2019

V. Soni, A. Chaudhuri , N. Brahmi, and A. Hadjadj



View Online



Export Citation



CrossMark



CAPTURE WHAT'S POSSIBLE
WITH OUR NEW PUBLISHING ACADEMY RESOURCES

Learn more 



Turbulent structures of shock-wave diffraction over 90° convex corner

Cite as: Phys. Fluids 31, 086103 (2019); doi: 10.1063/1.5113976

Submitted: 10 June 2019 • Accepted: 11 July 2019 •

Published Online: 12 August 2019



V. Soni,¹ A. Chaudhuri,^{2,a)}  N. Brahmi,¹ and A. Hadjadj¹

AFFILIATIONS

¹Normandie University, INSA of Rouen, CNRS, CORIA, 76000 Rouen, France

²Department of Civil Engineering and Energy Technology OsloMet—Oslo Metropolitan University, Pilestredet 35, PB 4, St. Olavs Plass, 0130 Oslo, Norway

^{a)}Electronic mail: arnab.chaudhuri@oslomet.no

ABSTRACT

The turbulent structures and long-time flow dynamics of shock diffraction over 90° convex corner associated with an incident shock Mach number $M_s = 1.5$ are investigated by large eddy simulation (LES). The average evolution of the core of the primary vortex is in agreement with the previous two dimensional studies. The Type-N wall shock structure is found to be in excellent agreement with the previous experimental data. The turbulent structures are well resolved and resemble those observed in the experimental findings. Subgrid scale dissipation and subgrid scale activity parameter are quantified to demonstrate the effectiveness of the LES. An analysis based on turbulent-nonturbulent interface reveals that locally incompressible regions exhibit the universal teardrop shape of the joint probability density function of the second and third invariants of the velocity gradient tensor. Stable focus stretching (SFS) structures dominate throughout the evolution in these regions. Stable node/saddle/saddle structures are found to be predominant at the early stage in locally compressed regions, and the flow structures evolve to more SFS structures at later stages. On the other hand, the locally expanded regions show a mostly unstable nature. From the turbulent kinetic energy, we found that the pressure dilatation remains important at the early stage, while turbulent diffusion becomes important at the later stage. Furthermore, the analysis of the resolved vorticity transport equation reveals that the stretching of vorticity due to compressibility and stretching of vorticity due to velocity gradients plays an important role compared to diffusion of vorticity due to viscosity as well as the baroclinic term.

Published under license by AIP Publishing. <https://doi.org/10.1063/1.5113976>

NOMENCLATURE

General description and validation

I	incident shock wave
DS	diffraction shock wave
EW	expansion shock wave
CS	contact surface
SL	shear layer
KHI	Kelvin-Helmholtz instabilities
V	vortex core
VV	viscous vortex
VS	vortex shock
LS	lambda shock

Local flow topology

P	first invariant of the velocity gradient tensor
Q	second invariant of the velocity gradient tensor

R	third invariant of the velocity gradient tensor
Q_w	second invariant of the rotation-rate tensor
UFC	unstable focus compressing
UN/S/S	unstable node/saddle/saddle
SN/S/S	stable node/saddle/saddle
SFS	stable focus stretching
SFC	stable focus compressing
UFS	unstable focus stretching

Vorticity transport equation (VTE)

VSC (\mathcal{V}_c)	stretching of vorticity due to compressibility
VSG (\mathcal{V}_g)	stretching/tilting of vorticity due to velocity gradients
\mathcal{B}	Baroclinic torque
DFV (\mathcal{D}_v)	diffusion of vorticity due to viscosity
\mathcal{E}	enstrophy

I. INTRODUCTION

Study of shock diffraction over various geometries has been an active research field for several decades. For example, Griffith and Bleakney¹ addressed the complexity involved in unsteady shock dynamics related to such shock-wave diffraction phenomenon in early 50's. Understanding shock diffraction is important for internal/external compressible flows involving the propagation of shock waves over solid surfaces, e.g., applications like mitigating shock/blast wave with designing effective shock resistant structures. The flow dynamics of these applications involves complex coupled interactions such as shock-shock, shock-vortex, vortex-vortex, and shock-turbulence interactions. Along with experimental approaches, with the advent of numerical techniques, numerical studies gained popularity for addressing intricate issues associated with such complex flow dynamics. Two-dimensional (2D) inviscid simulations²⁻⁵ are capable of resolving the general features associated with shock-wave diffraction. Most of the studies in the literature relied upon the inviscid predictions to establish the basic wave characteristics. Among these, Baum *et al.*⁴ presented a 2D numerical study of complex geometry canisters using an adaptive finite element based shock capturing scheme. Subsequently, several qualitative studies addressed the shock wave interaction with the compressible vortex associated with shock diffraction⁶⁻¹⁰ problems. Viscous effects are important to resolve the long-time evolution of shock-vortex dynamics and shock-boundary layer/shock-shear layer interactions. High-order scheme based numerical solvers equipped with robust shock capturing capabilities are essential to resolve the shock dynamics as well as the wide range of length/time scales of the turbulence. In this regard, several studies utilized high-order Weighed Essentially Non Oscillatory (WENO) based schemes¹¹⁻¹⁷ or Discontinuous spectral element method (DSEM) with artificial viscosity¹⁸⁻²⁰ to address complex flow features associated with shock diffraction, shock propagation, shock focusing, shock obstacle interaction, etc. Unsteady three-dimensional (3D) studies of shock diffraction are not abundant in the literature. Reeves and Skews²¹ studied the evolution of spiral vortex for 3D edges ("V," "inverted-V," "parabolic," and "inverted parabolic" types). A general and preliminary three-dimensional study of the merging of vortices resulting from shock diffraction and vortex shedding off a discontinuous edge is presented by Cooppan and Skews.²² Also, Skews and Bentley²³ addressed a 3D analysis of the merging of two diffracting shocks.

In a recent study,¹⁹ the authors revisited the shock diffraction over 90° convex corner and addressed some intricate features of resolving the viscous and turbulent flow features. The main issues related to the 2D numerical predictions of this flow dynamics are to address the experimentally observed (i) secondary viscous vortex associated with the wall shock interaction with the boundary layer and (ii) the shear layer behavior (see, e.g., Refs. 24 and 6 for detail of this canonical benchmark case). These are addressed with a high-order numerical scheme based predictions by Chaudhuri and Jacobs.¹⁹ It can be realized from the relatively recent experiments (e.g., Refs. 25 and 26) that the shear layer structures associated with the long-time evolution exhibit fine turbulent flow structures.

It is evident that 3D simulations and analysis are required to shed light into the turbulent structures and shear layer instabilities observed in these experiments. To the best of our knowledge,

analysis of 3D flow features associated with shock diffraction over sharp corners has never been reported before. The objective of this work is to perform large eddy simulation (LES) to explore the 3D turbulent flow structures and analyze the long-time behavior of the shock diffraction over 90° convex corner with incident shock Mach number $M_s = 1.5$. The paper is organized as follows. In Sec. III, a brief description of the methodology is described. The numerical setup is presented in Sec. II followed by the results and discussions in Sec. IV. Finally, conclusions are drawn in Sec. V.

II. PROBLEM SETUP

Moving shock wave of shock Mach number $M_s = 1.5$ is allowed to pass through a 90° convex corner having a rectangular cross section of 35 mm × 25 mm. The step height h is taken as 140 mm, and the step length is set to 25 mm. The problem setup of the simulation is shown in Fig. 1. The mesh resolution of the computational domain of 200 mm × 175 mm × 35 mm (length-height-width) is summarized in Table I. The initial location of the moving shock is positioned at 75% of the step length. Rankine-Hugoniot relations are used to set the initial conditions for left (shocked state) and right (stagnant state) states associated with the chosen M_s . Air is considered as working fluid, and the initial stagnant state is assigned with temperature $T = 288$ K and pressure $p = 101325$ Pa. The spanwise (z -direction) direction is considered as the homogeneous direction, and periodic boundary conditions are applied at these boundaries. The left and right boundaries (x -direction) are kept as the initial conditions, and simulations are executed avoiding any reflections from these boundaries. We apply the symmetry condition at the top boundary, and adiabatic no-slip boundary conditions are set for the remaining solid walls. To assign realistic velocity fluctuations, homogeneous isotropic turbulent velocity fluctuations are superimposed with the initial velocity field in the shocked gas region.

III. METHODOLOGY

We solve the filtered compressible Navier Stokes system of equations to simulate the diffraction of the moving shock, over a convex corner. The definition of any filtered quantity with a filtered function G_Δ and filter width $\Delta = (\Delta_x \times \Delta_y \times \Delta_z)^{1/3}$ is given by $\bar{\phi}(\bar{x}, t) = \int_{R^3} \phi(\bar{\eta}, t) G_\Delta(\bar{x} - \bar{\eta}) d\bar{\eta}$. Favre averaged quantities $\bar{\phi} = \overline{\rho\phi}/\bar{\rho}$ are used to reduce subgrid scale (SGS) terms. The in-house parallel compressible flow solver equipped with the immersed boundary method is used for this purpose. The fifth-order WENO scheme is used for inviscid fluxes, and the sixth-order central difference scheme is used for viscous fluxes. A third-order explicit Runge-Kutta method is used to advance in time. The SGS stress and SGS heat flux terms are closed by the wall adapting the local eddy viscosity (WALE) model. For brevity, the filtered governing equations, LES model, and the immersed boundary methodology are not presented here, and the details are available in our previous works.^{12,27-29} The immersed boundary method (we use trilinear interpolation; see Ref. 29) in 3D simulations and LES model constants are essentially similar to those mentioned in these references. The flow solver is validated with relevant standard benchmark problems and is reported in our previous works. It is to be noted that only resolved quantities are used for the analysis and discussions

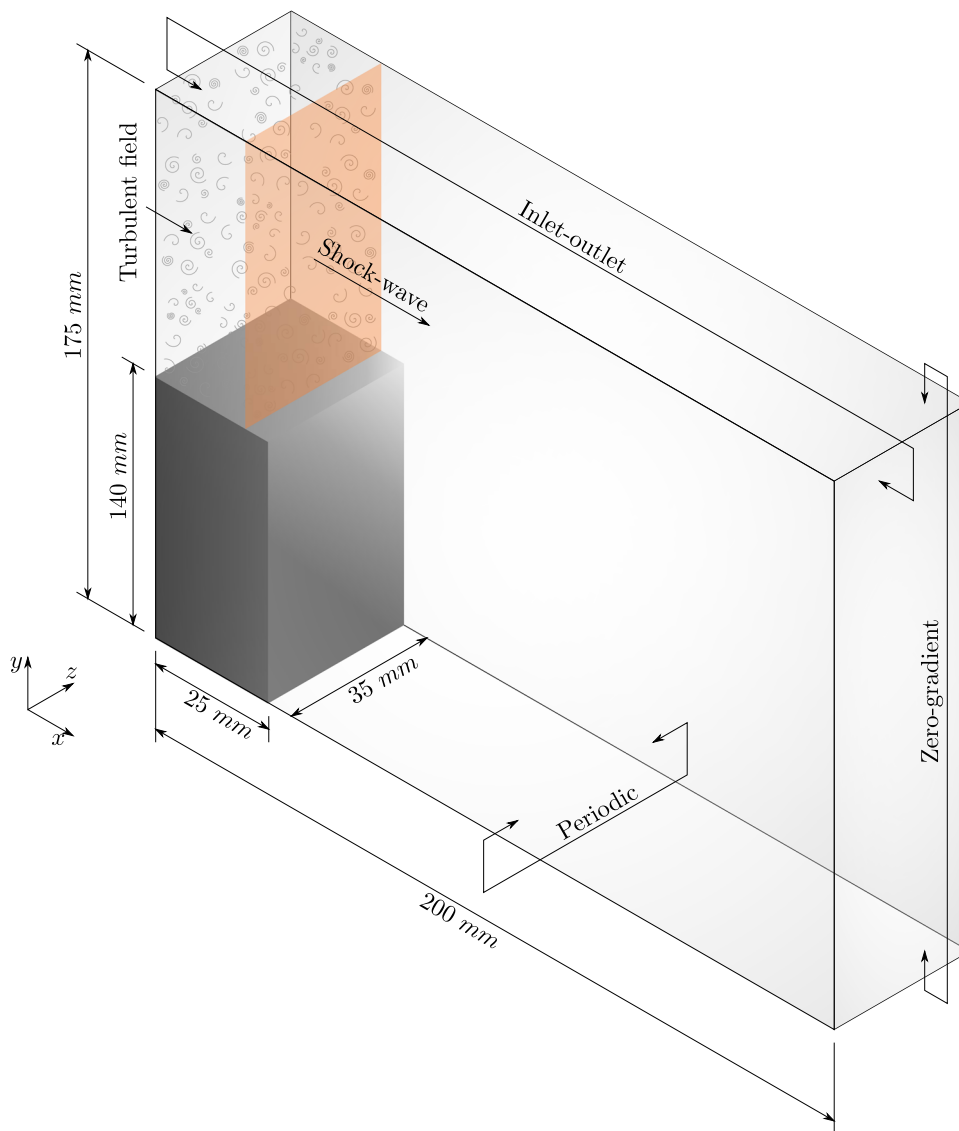


FIG. 1. Schematic diagram of the problem setup.

below. The resolved fluctuating component of any parameter is obtained by subtracting the spatially averaged (along the homogeneous z-direction) resolved quantity from the corresponding instantaneous resolved parameter as defined as $\phi'' = \tilde{\phi} - \langle \tilde{\phi}(x, y, t) \rangle$, where $\langle \tilde{\phi}(x, y, t) \rangle = \frac{1}{L_z} \int_{L_z} \tilde{\phi} dz$.

To reduce the complexity of the notation, the resolved quantities are expressed without overbar ($\overline{\cdot}$) or tilde ($\tilde{\cdot}$) notation in most of the discussions below. This means $\phi_i \equiv \phi_i$. To have better clarity,

TABLE I. Simulation parameters.

Total no. of meshes	$\Delta x (\mu\text{m})$	$\Delta y (\mu\text{m})$	$\Delta z (\mu\text{m})$	Final time $t (\mu\text{s})$
3.3×10^9	52.6	51.4	136.7	757.75

only the notations for the turbulent kinetic energy budget equation are presented with actual notations.

IV. RESULTS AND DISCUSSIONS

A. General description and validation

The shock diffraction over 90° diffraction corner is associated with complex coupled interactions like shock-vortex, shock-boundary layer, vortex-vortex, and shock-shock interactions. Studies in the literature show that, 2D Euler predictions sufficiently agree with the early stage of the general shock dynamics but suffers from inability to resolve secondary vortex formation due to boundary layer interactions with the wall shock. Nevertheless, high-resolution 2D Navier-Stokes simulations with consideration of viscous/turbulent effects can predict these behaviors well.^{19,29} This

canonical benchmark problem of diffraction is being studied in the literature by several authors, but no 3D numerical studies are available to account for the long-time behavior of turbulent flow structures. Experimental observations show existence of these 3D structures (see Refs. 25 and 26). The LES performed in this study demonstrates these structures. The early and later stages shock dynamics and the complex interactions are presented in Fig. 2 and compared favorably with the experimental results. Especially, the present LES resolved the intricate turbulent structures illustrated by the numerical schlieren pictures. A detailed analysis of turbulent flow features is presented in Secs. IV B–IV E.

The convective Mach number ($M_c = \frac{U_1 - U_c}{a_1} = \frac{U_c - U_2}{a_2}$) at various locations at $t = 757.75 \mu\text{s}$ is found to be 0.53 at A*, 0.43 at B*, 0.29 at C*, and 0.16 at D* (see Fig. 3 for the locations of the measurements of M_c). Here, $U_c = \frac{a_1 U_2 + a_2 U_1}{a_1 + a_2}$. Also, U_1 and U_2 are the free stream velocities across the shear layer, and a_1 and a_2 are the respective speeds of the sound. The shear layer behavior shows prominent compressibility effects near the diffraction corner (A*) and progressively shifts toward near incompressible regime around D*.

We analyze the sufficiency of the domain length in the homogeneous direction via two-point autocorrelation function given by

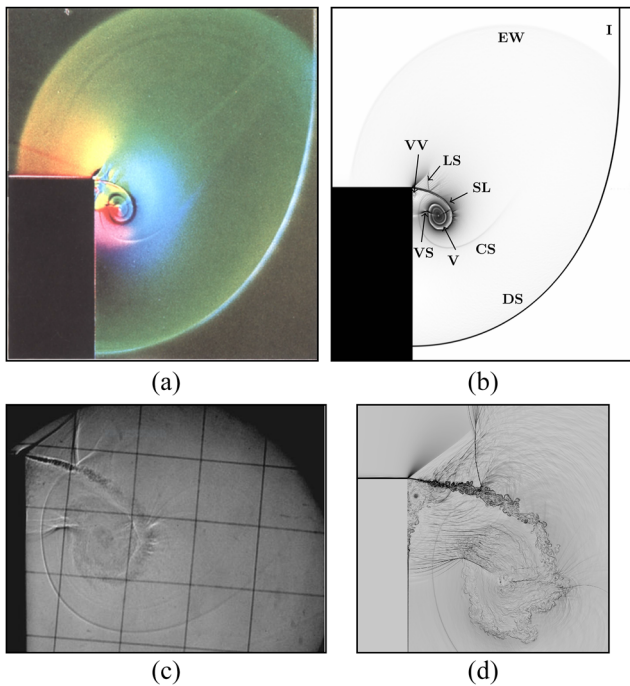


FIG. 2. Comparison of the flow features of the shock wave diffraction: top row: at early stage and bottom row: at later stage. See nomenclature. Figure (a) experiment, Takayama and Inoue.²⁴ [Reproduced with permission from K. Takayama and O. Inoue, “Shock wave diffraction over a 90 degree sharp corner—posters presented at 18th ISSW,” *Shock Waves* 1, 301–312 (1991). Copyright 1991 Springer-Verlag.] (b) Schlieren: present LES. Figure (c) experiment, Skews *et al.*²⁵ [Reproduced with permission from Skews *et al.*, “Shear layer behavior resulting from shock wave diffraction,” *Exp. Fluids* 52, 417–424 (2012). Copyright 2012 Springer-Verlag.] (d) Schlieren: present LES.

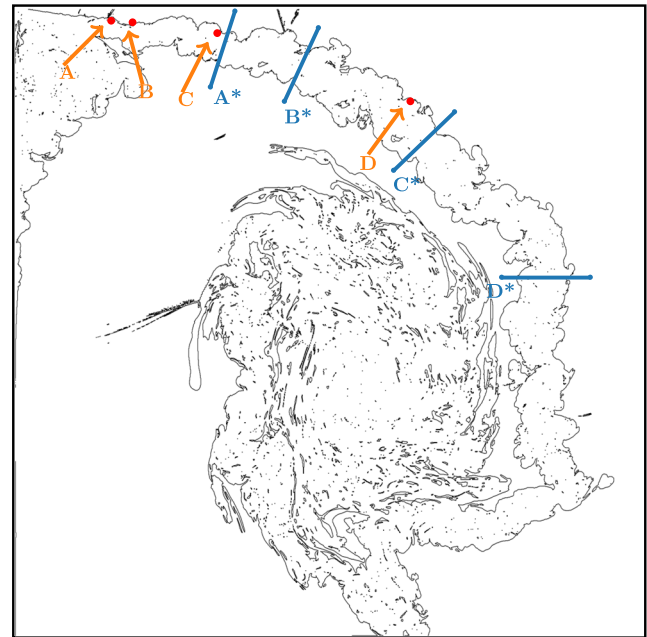


FIG. 3. Locations of probes/segments over a turbulent-nonturbulent interface (TNTI) contour for the computation of convective Mach number, two-point correlation, and normalized energy spectra.

$$R_{\phi\phi}(r_z) = \sum_{n=1}^{N_z} \phi_n'' \phi_{n+n_r}'' , \quad n_r = 0, \dots, N_z - 1; \quad r_z = n_r \Delta z. \quad (1)$$

Figure 4 shows the autocorrelation distributions for velocity fluctuations at different probe locations A to D (see Fig. 3). The curves degenerate to near zero values within the half of the domain length in the homogeneous direction. The domain size is thus sufficient enough so that the periodic boundary condition does not inhibit the turbulence in the spanwise z -direction.

The accuracy of the LES is further checked by computing the normalized energy spectra of the fluctuating velocity components. These are shown in Fig. 5 together with the $-5/3$ law. These spectra show similar behavior of the peak values and exhibit drop off of about two decades. The large turbulent scales of the flow features are well resolved by the current LES, and SGS dissipation takes into account the dissipation effects of very fine scales. The effectiveness of the WALE model and SGS activity are illustrated in Subsection IV B.

Figure 6 shows the locus of the vortex centroid and the comparison with the previous 2D numerical results of Sun and Takayama.⁶ The wall shock for the present case is of Type-N as classified in the work of Matsuo *et al.*³ Note that an excellent agreement of the shape of the wall shock with the experimental results of Skews³⁰ is predicted by the present simulation. The circulation, $\Gamma = \int_s \omega ds$, is computed over the 3D interaction region and is illustrated in Fig. 7. The circulation rate is nondimensionalized with the property of the air at the stagnant state, $RT = 287 \times 288 \text{ m}^2/\text{s}^2$. The nondimensional circulation is found to be attaining a saturation value of ≈ 1.2 . However, Sun and Takayama⁷ reported a circulation rate of 1.36 based on their 2D study.

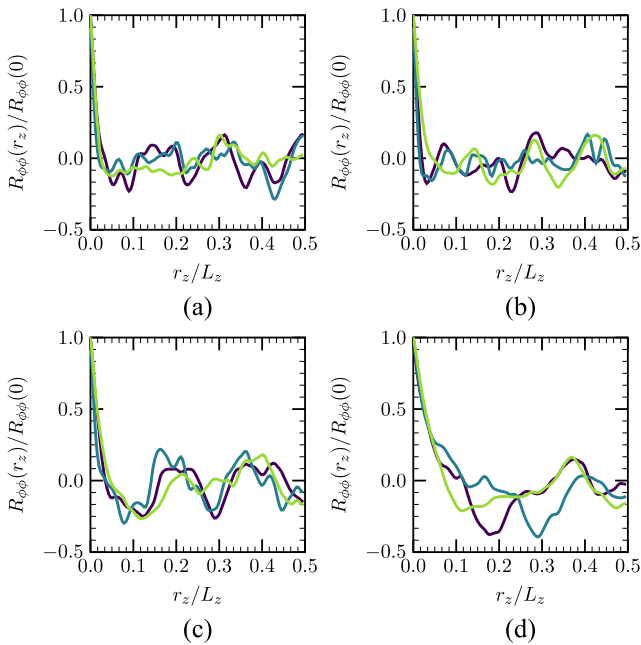


FIG. 4. Two-point correlation evaluation at $t = 757.75 \mu\text{s}$: (a) location A, (b) location B, (c) location C, and (d) location D. Violet solid curve: u , dark green solid curve: v , and light green solid curve: w .

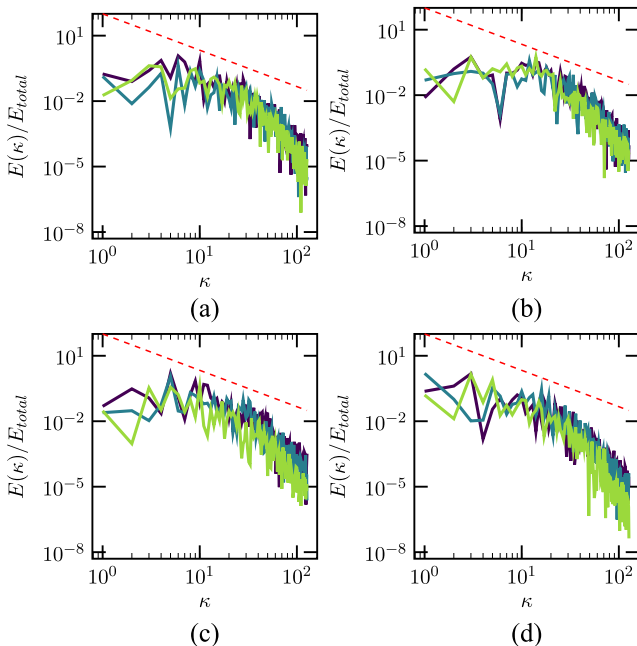


FIG. 5. Normalized energy spectra with wavenumber κ , at $t = 757.75 \mu\text{s}$ in the homogeneous direction: (a) location A, (b) location B, (c) location C, and (d) location D. Violet solid curve: u , dark green solid curve: v , light green solid curve: w , and red short-dashed curve: $-5/3$ law.

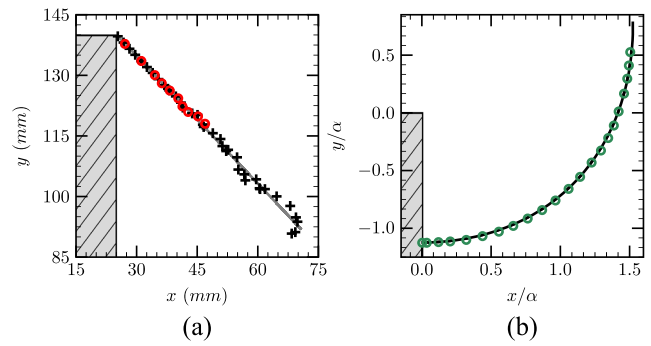


FIG. 6. (a) Location of the vortex centroid. Black plus sign: centroid path (simulation), gray solid curve: mean path, and red open circle: numerical data.⁶ (b) Diffracted shock wave location (here, $\alpha = a_0 t$, where a_0 is the speed of sound at the stagnate state). Black solid curve: simulation data and green open circle: experimental data.³⁰

The turbulent and nonturbulent regions for different turbulent flows are separated by a distinct boundary having several interesting characteristics like entrainment, abrupt changes in turbulence properties and intermittency. The shape of this interface is influenced by all scales of turbulence, in general. Vorticity norm or passive scalar concentration or concentration field can be used to define this turbulent-nonturbulent interface (TNTI).^{31–36} To do this, we use the mean magnitude of the vorticity at each x - y plane. The 30% of it is then set as the threshold value to define a TNTI parameter as $\text{TNTI}_z = 0.3|\bar{\omega}|_z$, $z = 1, \dots, N_z$. A location is considered inside the turbulent region if the magnitude of its local vorticity is higher than the TNTI_z in that x - y plane. Figure 3 depicts the inner turbulent region covered by the TNTI surface at $t = 757.75 \mu\text{s}$. The choice of the threshold value is intuitive, and these contours effectively identify the vortex dominated turbulent regions for further analysis. The irrotational engulfed pockets are also visible in this figure. Rotational dominated regions of the flow field can be illustrated from the normalized Q-criteria,^{37,38} $\Lambda = \frac{W_{ij}W_{ij} - S_{ij}S_{ij}}{W_{ij}W_{ij} + S_{ij}S_{ij}}$, where $S_{ij} = 1/2(\partial u_i/\partial x_j + \partial u_j/\partial x_i)$ is the strain-rate tensor and $W_{ij} = 1/2(\partial u_i/\partial x_j - \partial u_j/\partial x_i)$ is the rotation-rate tensor. The positive isosurfaces of Λ shown in Fig. 8 illustrate the vortex tubes and 3D turbulent flow features.

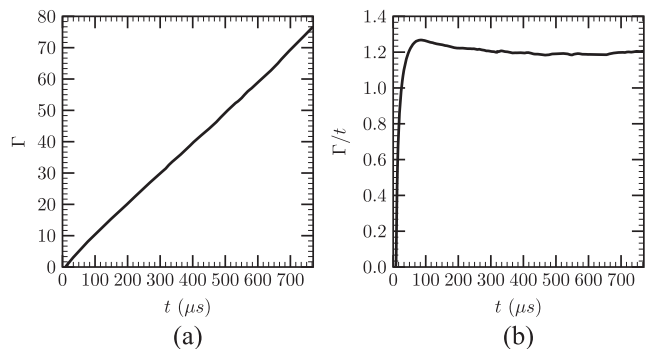


FIG. 7. Time evolution of (a) circulation (Γ) and (b) circulation rate (Γ/t).

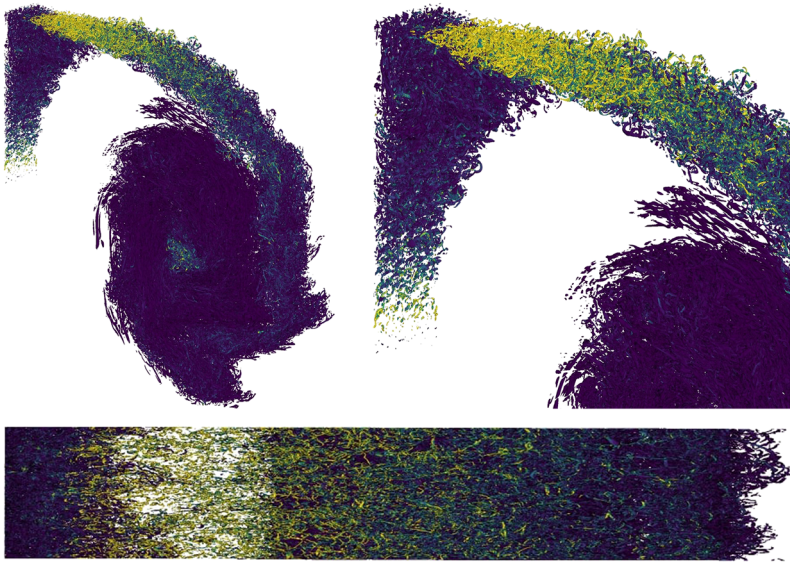


FIG. 8. Isosurfaces of $\Lambda = 0.5$ at $t = 757.75 \mu\text{s}$ colored with the enstrophy.

B. SGS model assessment

In this section, we present the relative contribution of SGS dissipation and assess the effectiveness of the WALE model. The ratio of μ_{sgs}/μ is the measure of effectiveness of the LES model. Figure 9 shows the time evolution of the spatially averaged contours of μ_{sgs}/μ (averaged in the homogeneous z -direction) in the interaction zone. The ratio, $\mu_{sgs}/\mu \leq 5$, indicates that the grid resolution and the contribution of SGS viscosity are in the acceptable range for well resolved LES. The SGS modeled dissipation ϵ_{sgs} can be defined as²⁸ the summation of contribution of fluctuating flow-field to SGS dissipation and the contribution of mean flow-field to SGS dissipation as

$$\epsilon_{sgs} = \epsilon''_{sgs} + \epsilon_{(sgs)}. \tag{2}$$

The contribution of fluctuating flow-field to SGS dissipation approximated as

$$\epsilon''_{sgs} \approx -2\langle \mu_{sgs} S''_{ij} S''_{ij} \rangle, \tag{3}$$

where $S''_{ij} = \frac{1}{2} \left(\frac{\partial u''_i}{\partial x_j} + \frac{\partial u''_j}{\partial x_i} \right)$ and $S''_{ij}{}^* = S''_{ij} - \frac{1}{3} S''_{kk} \delta_{ij}$.

The contribution of mean flow-field to SGS dissipation can be expressed as

$$\epsilon_{(sgs)} \approx -2\langle \mu_{sgs} \rangle \langle S_{ij}^* \rangle \langle S_{ij} \rangle, \tag{4}$$

where $\langle S_{ij} \rangle = \frac{1}{2} \left(\frac{\partial \langle u_i \rangle}{\partial x_j} + \frac{\partial \langle u_j \rangle}{\partial x_i} \right)$ and $\langle S_{ij}^* \rangle = \langle S_{ij} \rangle - \frac{1}{3} \langle S_{kk} \rangle \delta_{ij}$.

The details of these approximations can be found in the work of Ben-Nasr *et al.*²⁸ and Davidson.³⁹

Figure 10 shows the different SGS dissipation parameters (averaged in the homogeneous z -direction) in the interaction zone at different time instants. It can be seen from this figure that ϵ''_{sgs} contributes more toward ϵ_{sgs} compared to $\epsilon_{(sgs)}$. The contours of $\frac{\epsilon_{sgs}}{\epsilon}$ show a similar range of values of μ_{sgs}/μ as mentioned before. This corroborates the fact that the mesh resolution in the shear layer region is sufficient for this LES study. The modeling effectivity of a LES can also be quantified with the SGS activity parameter as defined by

$$\zeta = \frac{\epsilon_{sgs}}{\epsilon_{sgs} + \epsilon}, \tag{5}$$

where the resolved molecular dissipation $\epsilon = \left\langle \tau''_{ij} \frac{\partial u''_i}{\partial x_j} \right\rangle$. Evidently, $0 \leq \zeta < 1$, and the lower the value of ζ the more resolved is the LES. It could be noted that the vortex core region is very well resolved by the current LES. These are in accordance with the 3D flow

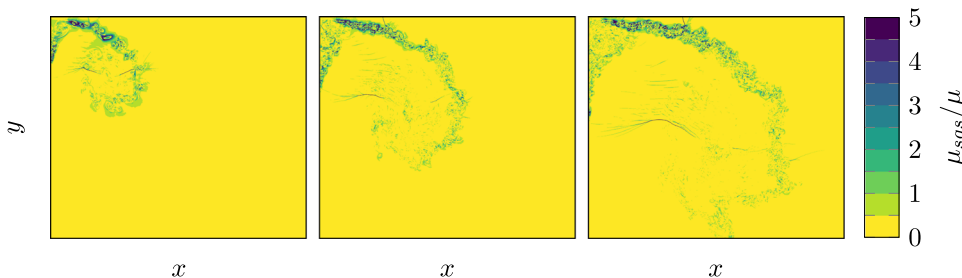


FIG. 9. μ_{sgs}/μ of a slice at $t = 339.75, 537.75, \text{ and } 757.75 \mu\text{s}$ column-wise, respectively.

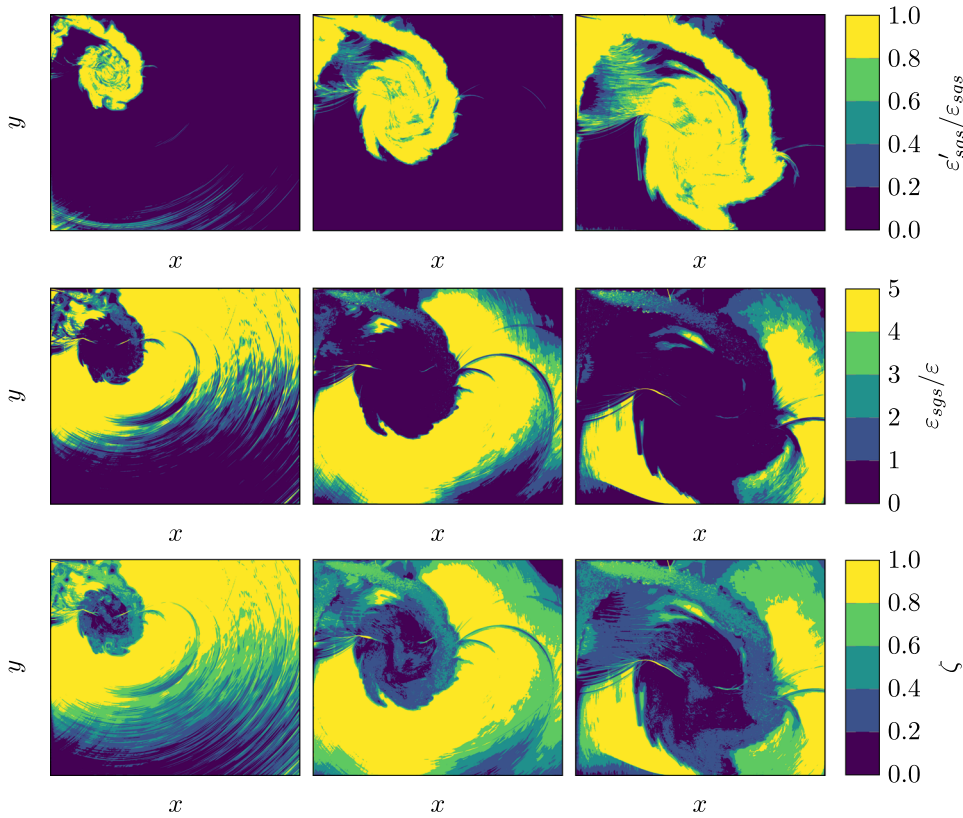


FIG. 10. Different subgrid-scale dissipation terms at $t = 339.75, 537.75,$ and $757.75 \mu\text{s}$ column-wise, respectively.

visualization of resolved flow structures illustrated with the isosurfaces of $\Lambda = 0.5$ in Fig. 8.

C. Analysis on the local flow topology

The flow topology analysis based on the turbulent/nonturbulent interface (TNTI) which separates the inner core of the turbulent region from the neighborhood of the irrotational regions is much revealing and enriching to characterize the zonal turbulent flow structures. The literature shows that the locally compressed regions in a turbulent flow field are dominated by stable topological structures, while the locally expanded regions are mainly unstable in nature and more dissipative. In this section, we present the flow topology associated with the dynamics of the shear layer at the 90° diffraction corner. The invariants of the velocity (resolved) gradient tensor ($P, Q,$ and R) are given by

$$P = -S_{ij}, \tag{6}$$

$$Q = \frac{1}{2}(P^2 - S_{ij}S_{ji} - W_{ij}W_{ji}), \tag{7}$$

$$R = \frac{1}{3}(-P^3 + 3PQ - S_{ij}S_{jk}S_{ki} - 3W_{ij}W_{jk}S_{ki}), \tag{8}$$

where S_{ij} and W_{ij} are strain-rate tensor and rotation-rate tensor as defined before.

It is well known that the $P - Q - R$ space is divided into several regions.⁴⁰⁻⁴⁵ The discriminant surface \mathcal{L}_1 , of the characteristic equation of the eigenvalues of the velocity gradient tensor, separates the

region of real and complex eigenvalues. This can be further split into \mathcal{L}_{1a} and \mathcal{L}_{1b} . All eigenvalues are real and equal at a location where these surfaces form a cusp. On the other hand, purely imaginary eigenvalues lie on the surface \mathcal{L}_2 [see Eq. (13)].

The second invariant of W_{ij} is given by

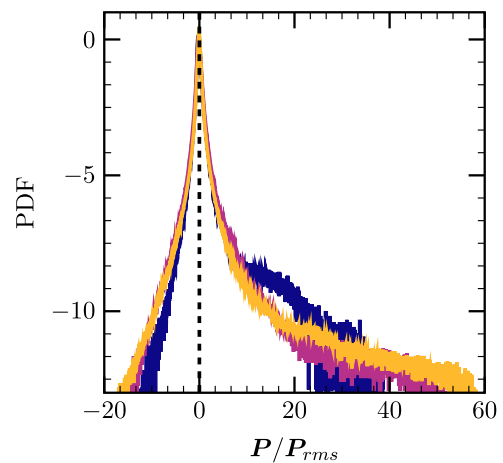


FIG. 11. PDF plot of the normalized first invariant of velocity gradient tensor in the entire turbulent region at $t = 251.75$ (violet solid curve), 449.75 (pink solid curve), and $757.75 \mu\text{s}$ (yellow solid curve).

TABLE II. Quantification of the flow topology enclosed by TNTI as a percentage of their sample size.

Dilatation	Quantity			UFC	UN/S/S	SN/S/S	SFS	SFC	UFS
	Time (μs)	(% of TNTI)	Sample ($\times 10^6$)						
$P = 0 \pm 0.05$	251.75	10.4	2.7	5.0	6.3	7.8	80.7
	449.75	9.8	8.5	3.2	3.7	2.2	90.9
	757.75	14	33.4	1.1	1.6	1.6	95.6
$P = 3 \pm 0.25$	251.75	0.2	0.05	11.6	7.1	48.1	21.8	9.8	...
	449.75	0.3	0.2	12.3	10.4	24.8	44.5	6.9	...
	757.75	0.2	0.4	10.8	10.2	17.2	55.9	5.8	...
$P = -3 \pm 0.25$	251.75	0.1	0.03	18.7	25.1	4.7	24.8	...	23.9
	449.75	0.2	0.2	17.7	30.8	2.6	30.7	...	16.9
	757.75	0.1	0.3	16.9	34.1	3.3	31.1	...	12.9

$$\mathbf{Q}_w = -\frac{1}{2} W_{ij} W_{ji}. \quad (9)$$

The surfaces dividing the $P - Q - R$ space are

$$\mathcal{L}_1 = 27R^2 + (4P^3 - 18PQ)R + (4Q^3 - P^2Q^2) = 0, \quad (10)$$

$$\mathcal{L}_{1a} = \frac{1}{3}P\left(Q - \frac{2}{9}P^2\right) - \frac{2}{27}(-3Q + P^2)^{3/2} - R = 0, \quad (11)$$

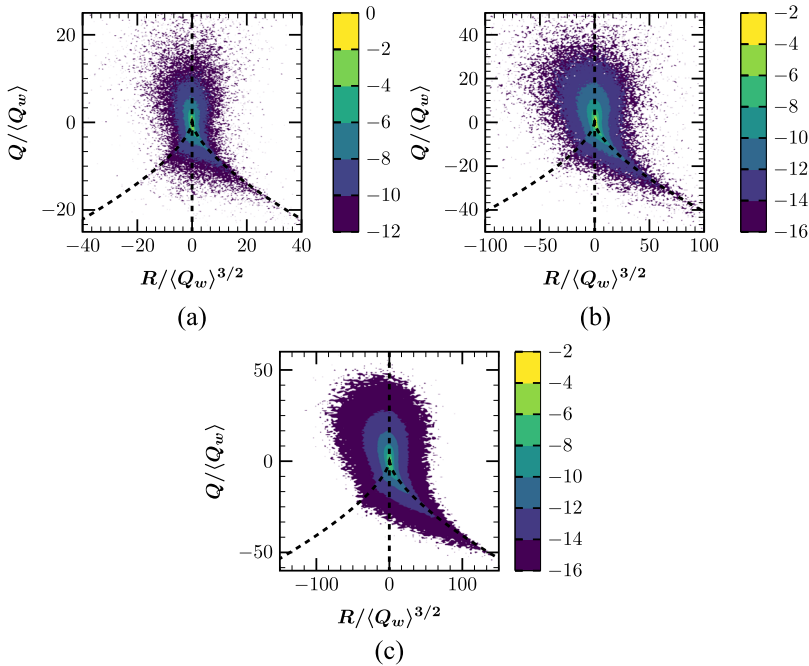
$$\mathcal{L}_{1b} = \frac{1}{3}P\left(Q - \frac{2}{9}P^2\right) + \frac{2}{27}(-3Q + P^2)^{3/2} - R = 0, \quad (12)$$

$$\mathcal{L}_2 = PQ - R = 0. \quad (13)$$

We summarize the nomenclature of the invariants and various 3D critical points in the nomenclature section.

The evolution of the probability density function (PDF) of the first invariant of the velocity gradient tensor is shown in Fig. 11. A

self-similar behavior with highly peaked distribution has been found. A large positive skewness of the distributions clearly depicts the similar behavior observed in the compressible isotropic turbulence and compressible mixing layer turbulence of the literature.⁴² The JPFDs of the $Q - R$ are shown for constant P planes. Three representative values of P are chosen to distinguish the features of locally incompressible, compressed, and expanded regions in the flow-field. Here, Q and R are normalized with Q_w and $Q_w^{3/2}$ in these figures. Table II summarizes all the quantities of the local flow topology for different dilatation levels at different time instants. Evidently, the sample size is large at a later time instant. Note that the percentage of TNTI is large for $P = 0$ compared to locally compressed and expansion regions. This corroborates with highly peaked distribution of PDF of P mentioned before. For incompressible turbulent flows ($P = 0$), the JPFD of second and third invariants (Q and R) of


FIG. 12. JPFD plot of the normalized second and third invariants of velocity gradient tensor in the entire turbulent (TNTI) region at $t = 251.75, 449.75,$ and $757.75 \mu\text{s}$ for $P = 0 \pm 0.05$.

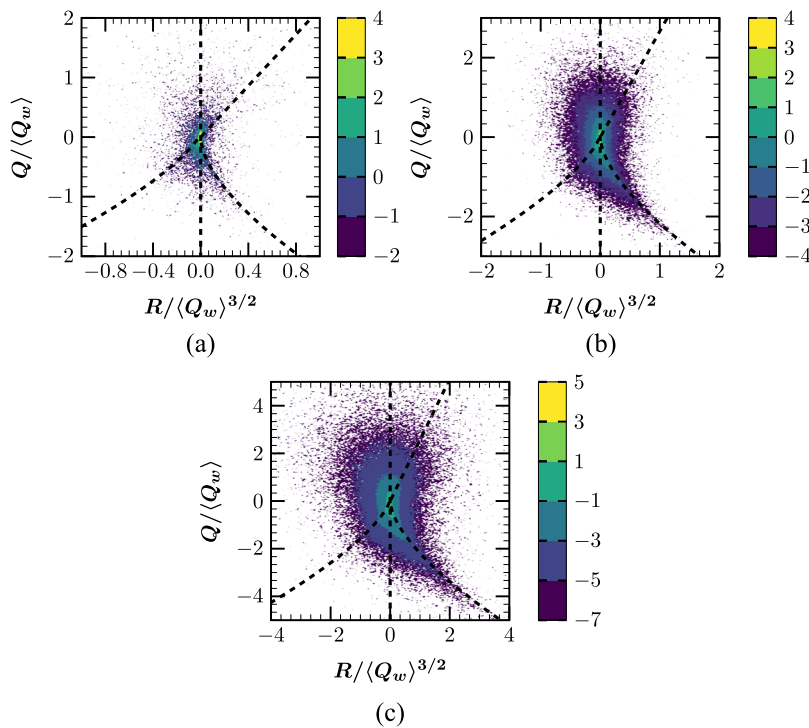


FIG. 13. JPDF plot of the normalized second and third invariants of velocity gradient tensor in the entire turbulent (TNTI) region at $t = 251.75, 449.75,$ and $757.75 \mu\text{s}$ for $P = 3 \pm 0.25$.

the velocity gradient tensor exhibits a typical tear drop shape (see Fig. 12). This signifies the universal small-scale structures of turbulence. The similar universal tear drop shape is also being found for compressible flows when the JPDF of second and third invariants

of the anisotropic part of the deformation rate tensor is analyzed. This is similar to the characteristics of incompressible turbulence, compressible isotropic turbulence, compressible turbulent boundary layer, and compressible mixing layer turbulence. Clearly, the SFS

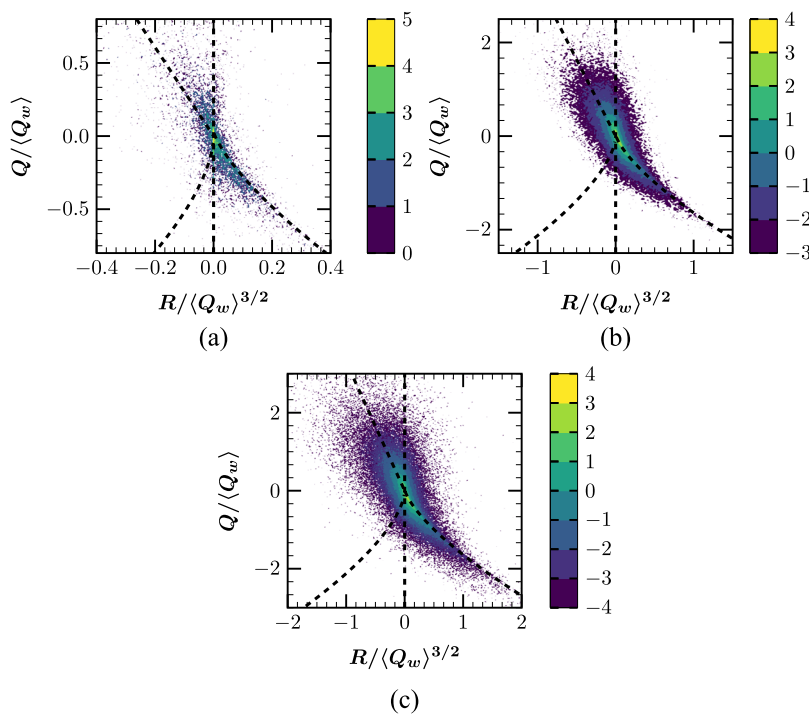


FIG. 14. JPDF plot of the normalized second and third invariants of velocity gradient tensor in the entire turbulent (TNTI) region at $t = 251.75, 449.75,$ and $757.75 \mu\text{s}$ for $P = -3 \pm 0.05$.

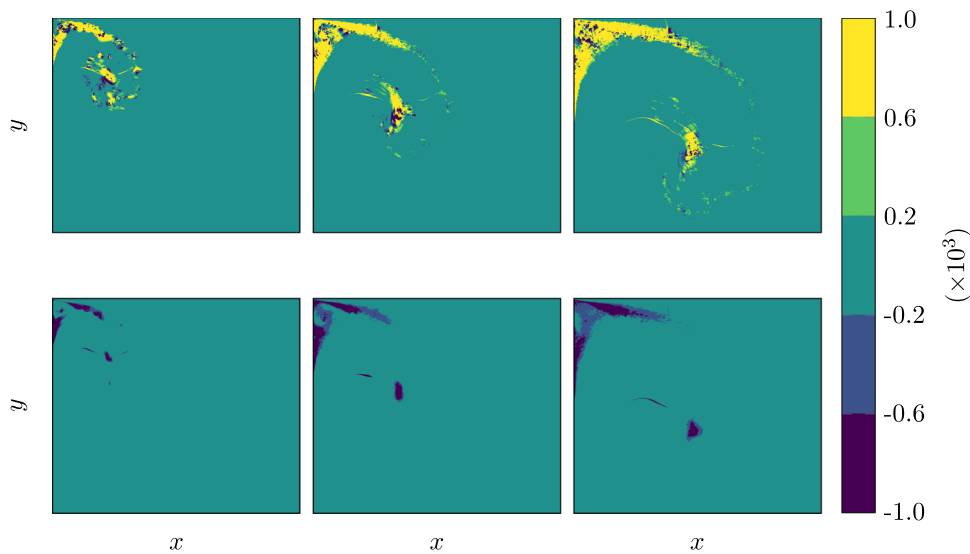


FIG. 15. TKE budget. Row-wise (top-to-bottom): production and dissipation terms. Column-wise (left-to-right): $t = 339.75, 537.75,$ and $757.75 \mu s$.

structure dominates throughout the evolution with an increasing trend of the SFS structure with time (95.5% at $757.75 \mu s$).

Figure 13 depicts JPDFs of $Q - R$ for locally compressed regions. The shape of these distributions evolves to nearly tear drop shape. However, it can be seen from Table II, that a dramatic distribution of the topologies is existent. Initially, we observe dominant

nonfocal stable structures (48.1% of SN/S/S). Most of the structures remain stable for compressed regions. Nevertheless, the unstable structures are also found to be present. The initial SN/S/S structures shift toward SFS structures. Although, there exist some more unstable structures compared to locally incompressible regions, the stable structures are predominant in locally compressed regions.

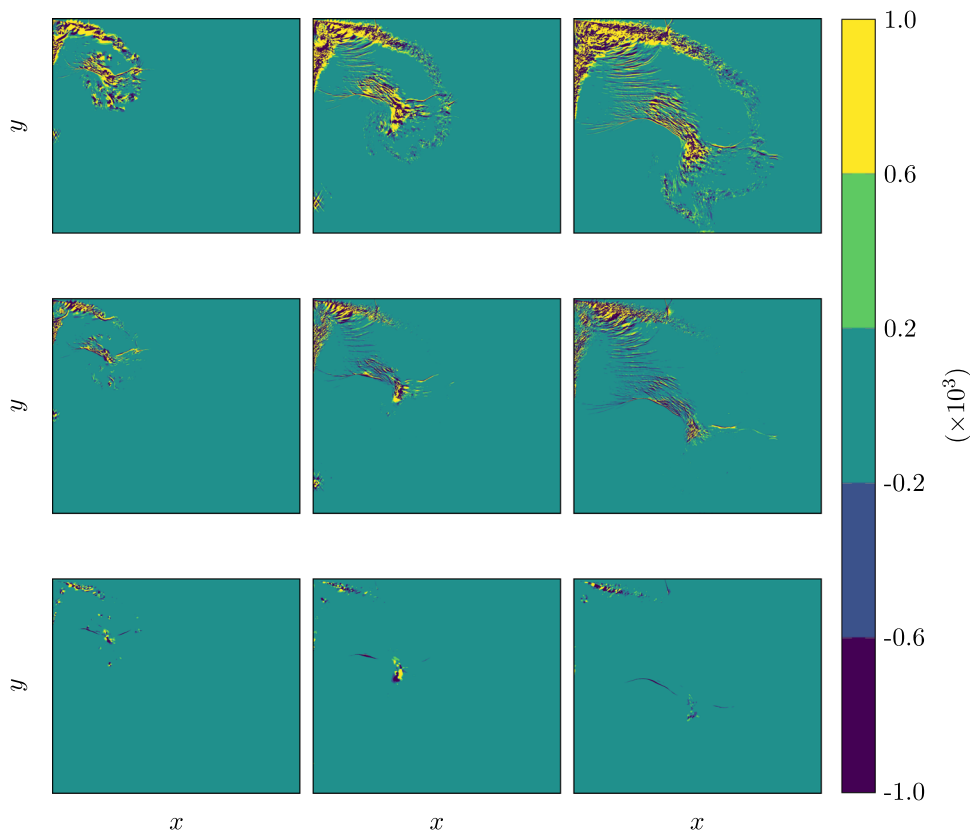


FIG. 16. TKE budget. Row-wise (top-to-bottom): diffusion, pressure-dilatation, and pressure-work terms. Column-wise (left-to-right): $t = 339.75, 537.75,$ and $757.75 \mu s$.

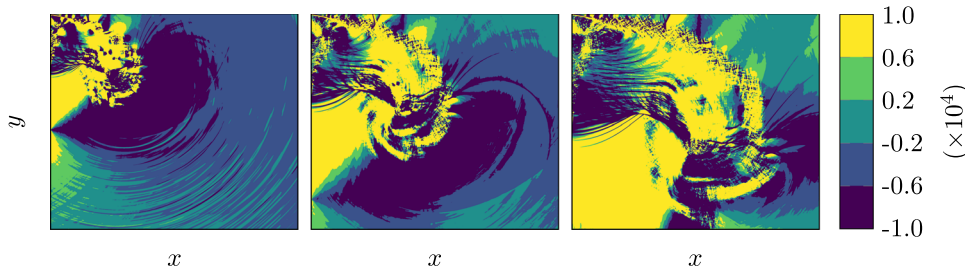


FIG. 17. TKE budget—advection term. Column-wise (left-to-right): $t = 339.75, 537.75,$ and $757.75 \mu\text{s}$.

Figure 14 shows the JPFDs for locally expanded regions. The distributions are found to be skewed toward the surface \mathcal{L}_2 , and most of the flow structures show unstable nature. The present analysis reveals the absence of UFS for the locally compressed region and the absence of SFC for locally expanded regions. UN/S/S structures eventually become predominant in these regions. The unstable structures indeed become significant for locally expanded regions. It can be realized that the local streamlines in stable topologies are convergent toward critical points, and for unstable topologies, the local streamlines are divergent from the critical points.

D. Analysis of the turbulent kinetic energy

The Favre averaged transport equation of turbulent kinetic energy (TKE) is given by

$$\begin{aligned} \frac{\partial \bar{\rho}k}{\partial t} + \underbrace{\frac{\partial \bar{\rho} \tilde{u}_j k}{\partial x_j}}_{\mathcal{A}} = & \underbrace{-\langle \rho u_i'' u_j'' \rangle \frac{\partial \tilde{u}_i}{\partial x_j}}_{\mathcal{P}} - \underbrace{\left\langle \tau_{ji} \frac{\partial u_i''}{\partial x_j} \right\rangle}_{\mathcal{D}} \\ & + \underbrace{\frac{\partial}{\partial x_j} \left(\langle \tau_{ji} u_i'' \rangle - \left\langle \rho u_j'' \frac{1}{2} u_i'' u_i'' \right\rangle - \langle p' u_j'' \rangle \right)}_{\mathcal{D}_f} \\ & - \underbrace{\langle u_i'' \rangle \frac{\partial \bar{p}}{\partial x_i}}_{\mathcal{P}_w} + \underbrace{\left\langle p' \frac{\partial u_i''}{\partial x_i} \right\rangle}_{\mathcal{P}_d}, \end{aligned} \quad (14)$$

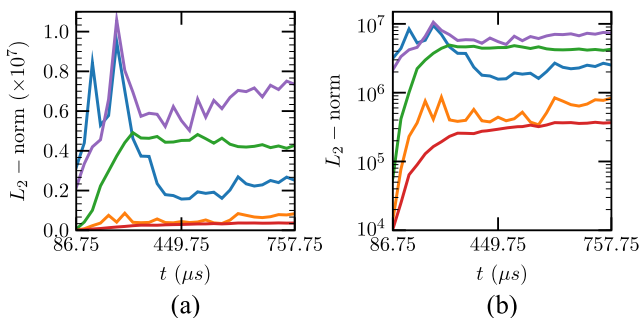


FIG. 18. Norm of TKE budget terms as a function of time (a) linear-scale and (b) logarithmic-scale. Blue solid curve: pressure-dilatation, orange solid curve: pressure-work, green solid curve: production, red solid curve: dissipation, and violet solid curve: diffusion.

where \mathcal{P} is the production term, \mathcal{D} is the dissipation term, \mathcal{D}_f is the diffusion term, \mathcal{P}_w is the pressure-work term, \mathcal{P}_d is the pressure-dilatation term, and \mathcal{A} is the advection term. Note that we kept the overbar $(\bar{\cdot})$ or tilde $(\tilde{\cdot})$ notation here for better clarity.

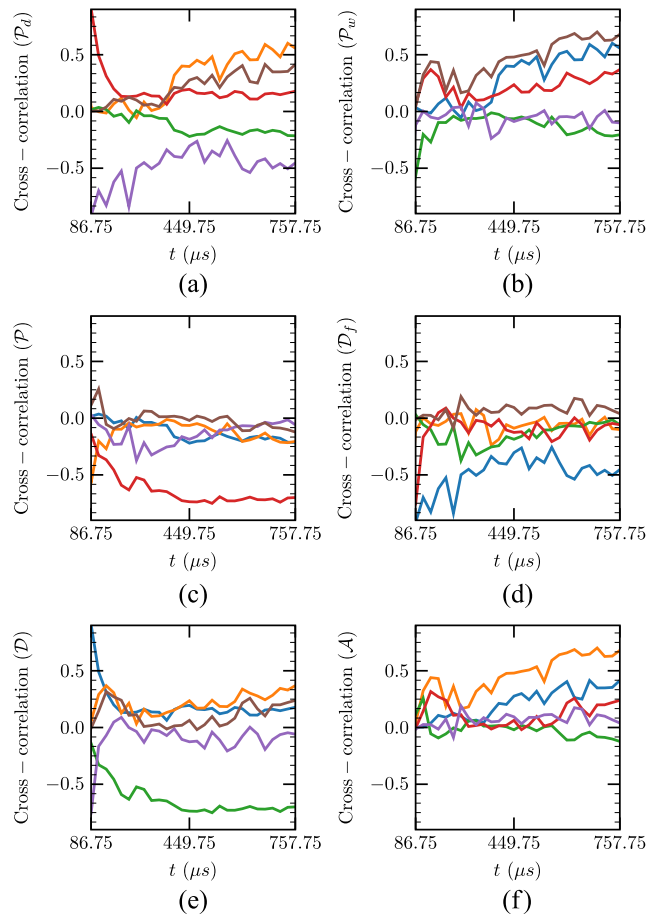


FIG. 19. Spatial cross-correlation of (a) pressure-dilatation (\mathcal{P}_d), (b) pressure-work (\mathcal{P}_w), (c) production (\mathcal{P}), (d) diffusion (\mathcal{D}_f), (e) dissipation (\mathcal{D}), and (f) advection (\mathcal{A}) terms of TKE budget with each other in time. Blue solid curve: pressure-dilatation, orange solid curve: pressure-work, green solid curve: production, red solid curve: dissipation, violet solid curve: diffusion, and brown solid curve: advection.

The spatially averaged contours of these resolved terms are shown in Figs. 15–17. The behavior of the TKE budget terms of the shear layer region is found to be typically similar to the compressible mixing layers (see Ref. 38). These contours also show the out of equilibrium behavior of the turbulent flow linked with the transient flow evolution. The pressure dilatation and pressure work terms are associated with the regions of the shear layer near the diffraction corners (having high convective Mach numbers) as well as regions where the interactions of the shocklets and the core of the vortex are significant. It can be seen that sporadic patches of negative production of turbulent kinetic energy are also predicted. These are associated with the regions with shear layer/vortex interactions with local compressions/expansions.^{27,46,47} We analyze the time evolution of the magnitude of these terms and their cross-correlations within the spatially averaged two dimensional turbulent region bounded by

the TNTI. These are shown in Figs. 18 and 19. At the early stage, the pressure dilatation term remains important, and the diffusion term plays a major role in the later stage. Diffusion, production, and pressure dilatation terms are found to be nearly one order of magnitude higher than pressure work and dissipation. Note that the pressure dilatation is more correlated with dissipation term at the beginning and evolves to a state with more correlated with pressure work at the later stage. The overall anticorrelation is evident between production and dissipation terms. Pressure dilatation and pressure work remain linked with dissipation. Noticeably, the diffusion term is found to be anticorrelated with the pressure dilatation term throughout the evolution. It can be realized that the diffusion terms interact with the outer regions of the shear layer through the edges of the shear layer. The advection term is found to be predominantly linked with pressure work apart from the other terms.

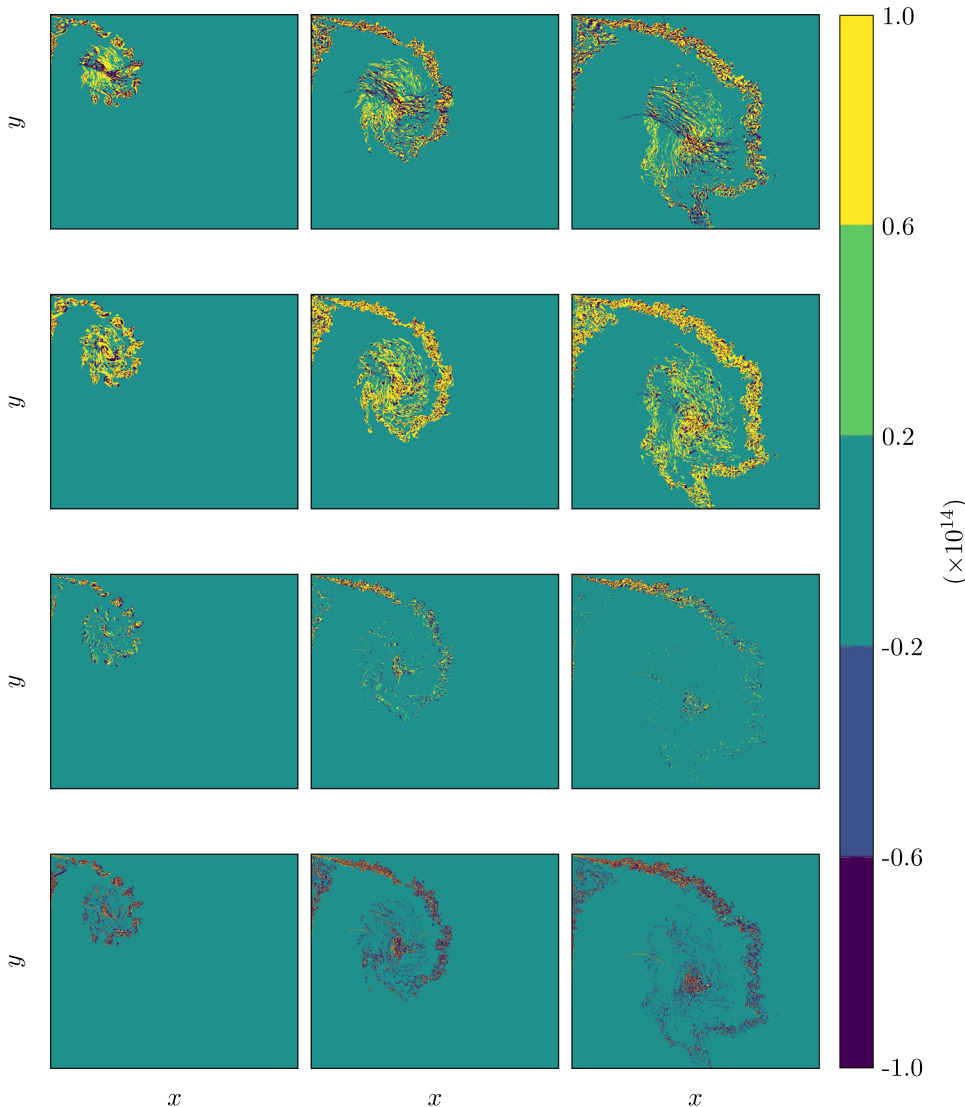


FIG. 20. VTE budget. Row-wise (top-to-bottom): VSC, VSG, baroclinic, and DFV terms. Column-wise (left-to-right): $t = 339.75, 537.75, \text{ and } 757.75 \mu s$.

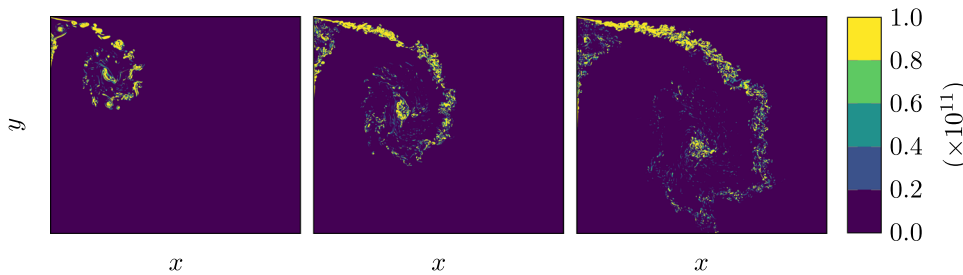


FIG. 21. Enstrophy contour. Column-wise (left-to-right): $t = 339.75, 537.75,$ and $757.75 \mu\text{s}$.

E. Analysis of the vorticity transport equation

We further analyze the budget terms of the mean vorticity transport equation [Eq. (15)] to shed light into the large scale structures and the mechanism of the complex flow evolution associated with the shock diffraction phenomena. The contribution of SGS terms can be assumed to be negligible for the mutual interactions among the relatively large vortical structures. The nomenclature of the different terms of the transport equation is summarized in the nomenclature section,

$$\frac{\partial \boldsymbol{\omega}}{\partial t} + (\mathbf{u} \cdot \nabla) \boldsymbol{\omega} = \underbrace{(\boldsymbol{\omega} \cdot \nabla) \mathbf{u}}_{V_g} - \underbrace{\boldsymbol{\omega} (\nabla \cdot \mathbf{u})}_{V_c} + \underbrace{\frac{1}{\rho^2} \nabla \rho \times \nabla p + \nabla \times \left(\frac{\nabla \cdot \boldsymbol{\tau}}{\rho} \right)}_B \underbrace{\phantom{\frac{1}{\rho^2} \nabla \rho \times \nabla p + \nabla \times \left(\frac{\nabla \cdot \boldsymbol{\tau}}{\rho} \right)}}_{D_v} \quad (15)$$

The evolution of the contours of these terms is shown in Fig. 20. VSC, VSG, DFV, and baroclinic terms interplay during the evolution process. From the VSC contour, it is clear that there are locally stretched structures in the core region of the vortex due to compressibility effect arising from local regions of compression/expansion. The evolution of enstrophy is illustrated in Fig. 21. This corroborates to saturation of the magnitude of the enstrophy. The time evolution of the magnitude of these terms and their cross-correlations within the 3D turbulent region bounded by the TNTI are analyzed further. Note that the magnitude of the VSG term and VSC term is nearly one order of magnitude higher compared to the baroclinic term and DFV term (see Fig. 22). Indeed, VSG plays a major role transferring the turbulent energy from large scales to small scales in flows at high Reynolds number as found in the work of Cottet *et al.*⁴⁸

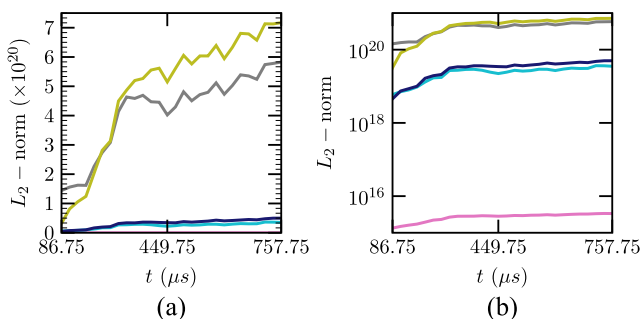


FIG. 22. Norm of VTE budget terms as a function of time (a) linear-scale and (b) logarithmic-scale. Pink solid curve: enstrophy, gray solid curve: VSC, light green solid curve: VSG, sky blue solid curve: baroclinic, and blue solid curve: DFV.

Positive correlation of VSG and VSC is observed (see Fig. 23). However, enstrophy is found to be predominantly correlated with VSG compared to VSC. Furthermore, viscous effects via DFV term are anticorrelated with enstrophy. DFV is also found to be anticorrelated with VSG, which is in accordance with the contours shown in Fig. 20.

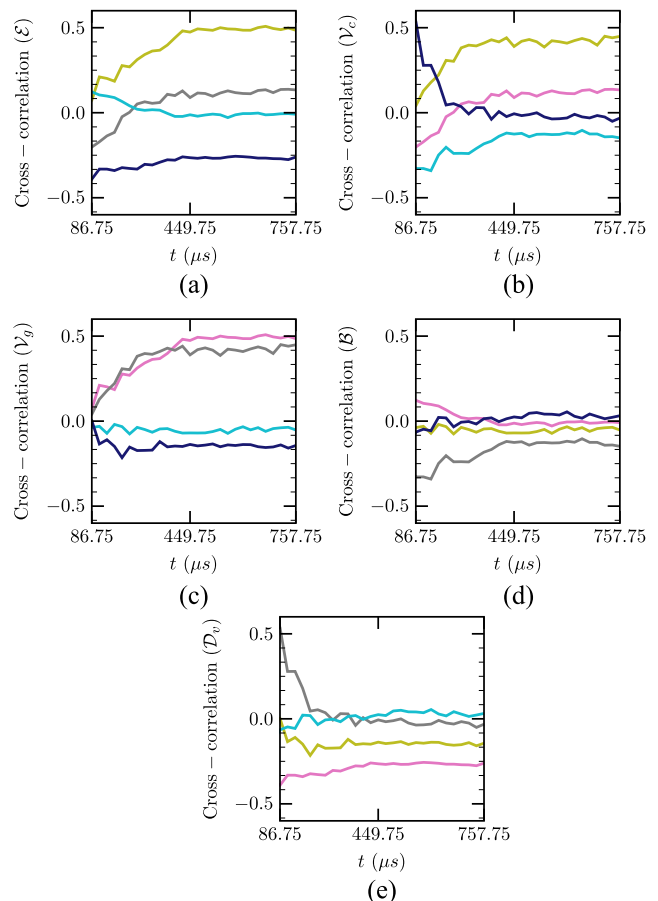


FIG. 23. Spatial cross-correlation of (a) enstrophy (\mathcal{E}), (b) VSC (V_c), (c) VSG (V_g), (d) baroclinic (B), and (e) DFV (D_v) terms of VTE budget with each other in time. Pink solid curve: enstrophy, gray solid curve: VSC, light green solid curve: VSG, sky blue solid curve: baroclinic, and blue solid curve: DFV.

V. CONCLUSION

In this work, we presented a 3D analysis of turbulent flow features originating from a shock wave diffraction over 90° convex corner that has never been attempted before. The intricate features of the viscous effects, shock boundary layer interactions, and shock shear layer interactions are well addressed by this analysis. LES with the WALE model together with high-order numerical schemes (fifth order WENO for inviscid, sixth order central differencing for viscous fluxes, and third order explicit Runge-Kutta scheme for the time advancement) is chosen to resolve the complex flow scales. The in-house parallel solver used 3.3×10^9 cells to resolve the flow structures. The general dynamics of vortex core and shape of the Type-N wall shock has been compared with the literature data³⁰ favorably. The chosen domain size in the spanwise direction is demonstrated to be sufficient enough through the behavior of autocorrelation functions. The effectiveness of the LES model and the mesh resolution characteristics are quantified by SGS viscosity and SGS dissipation. The 3D flow visualization with rotation dominated regions by normalized Q criteria shows the quality of the current well resolved LES. The 3D instantaneous field resembles the turbulent scale structures observed in the experimental findings.²⁵ We performed a flow topology analysis based on TNTI. The JPDFs of the second and third invariants (Q and R) of the velocity gradient tensor are used for constant (first invariant) P planes for this purpose. Locally, incompressible regions exhibit the teardrop shape of the PDF of Q and R indicating the universal nature of the resolved smaller scales of the turbulence. We found that SFS structures are dominating throughout the flow transients in these regions. SN/S/S structures remain predominant at the early stage in locally compressed regions, and at the later stage, the flow structures evolve to more SFS structures. Although unstable structures are found to be present relatively more compared to locally incompressible regions. On the other hand, we found mostly unstable structures at the locally expanded regions. The present analysis also reveals the absence of UFS for locally compressed region and the absence of SFC for locally expanded regions. Neglecting the SGS contributions, the turbulent kinetic energy budget terms are analyzed with only resolved parameters. This reveals that the pressure dilatation is important at the early stage, while turbulent diffusion becomes important at later stages and the diffusion term exhibits anticorrelation with the pressure dilatation term throughout the flow evolution. Furthermore, the relative contribution of the constituent terms of the resolved mean vorticity transport equation is analyzed. The VSC and VSG plays an important role compared to DFV, and baroclinic term and enstrophy are predominantly correlated with VSG compared to VSC.

The 2D viscous simulations of shock-wave diffraction over 90° sharp corner with a high resolution numerical scheme can predict the basic shock diffraction wave pattern, main vortex, secondary viscous vortex associated with the wall shock interaction with the boundary layer, shear layer, and lambda shocks observed in the experiments specially at the early stage of the evolution. However, 2D simulations are limited to resolve the inherent 3D nature of the turbulent flow features and together with the small-scale dissipation. The present 3D LES captures the 3D turbulent scales, embedded shocks/shocklets within the main vortex and the shear layer behavior and boundary layer interactions in the viscous vortex region. The spatio-temporal growth of the shear layer is strongly influenced by

the lambda shock as well as by the counterclockwise rotating viscous vortex near the diffraction corner. Apparently, the lambda-shock-shear-layer interaction at the upper side of the shear layer is more intense than that of the interaction of the contact surface at the bottom side of the shear layer. Note that the foot of the lambda shock more effectively perturbs the shear layer and increases its growth. This aspect is clearly resolved in the present LES. The shape and large-scale structures of the turbulent envelop at the wall viscous vortex region is also satisfactorily predicted by the LES. A further investigation regarding the mechanism and possible influence (upstream and downstream) of the contact surface at the underside of the shear layer could be addressed in future work.

Future works will be undertaken to address the performance of different LES models resolving this complex flow dynamics. A detailed analysis of the local entrainment across the TNTI can be explored for the compressible turbulent shear layer. The present LES is performed with 3×10^9 mesh points and can be considered as well resolved; however, further ensemble averaging could be attempted²⁷ with phase-incoherence in the initial isotropic turbulence to make stable flow statistics and detailed analysis toward the local mechanisms of the complex evolution. From the large-scale tests of Skews *et al.*,²⁵ it appears that several lambda shocks could play an important role toward large-scale KH instabilities at the later stage of the shear layer development. Also, the onset of the decay of the turbulence in the viscous vortex zone due to viscous dissipation is evident from the experimental findings. These long-time flow features could be investigated further to enhance the understanding of the complex flow dynamics.

ACKNOWLEDGMENTS

This study was supported by the BIOENGINE project, which is funded by the European Regional Development Fund (ERDF) and the Regional Council of Normandie under Contract No. HN-0002484. This work was performed using computing resources from Centre Régional Informatique et d'Applications Numériques de Normandie (CRIANN), Rouen, France.

REFERENCES

- 1 W. C. Griffith and W. Bleakney, "Shock waves in gases," *Am. J. Phys.* **22**, 597–612 (1954).
- 2 I. I. Glass, J. Kaca, D. L. Zhang, H. M. Glaz, J. B. Bell, J. A. Trangenstein, and J. P. Collins, "Diffraction of planar shock waves over half-diamond and semicircular cylinders: An experimental and numerical comparison," *AIP Conf. Proc.* **208**, 246–251 (1990).
- 3 K. Matsuo, T. Aoki, and H. Kashimura, "Diffraction of a shock wave around a convex corner," *AIP Conf. Proc.* **208**, 252–257 (1990).
- 4 J. D. Baum, E. Loth, and R. Löhner, "Numerical simulation of shock interaction with complex geometry canisters," *AIP Conf. Proc.* **208**, 909–914 (1990).
- 5 S. Sivier, E. Loth, J. Baum, and R. Löhner, "Vorticity produced by shock wave diffraction," *Shock Waves* **2**, 31–41 (1992).
- 6 M. Sun and K. Takayama, "A note on numerical simulation of vortical structures in shock diffraction," *Shock Waves* **13**, 25–32 (2003).
- 7 M. Sun and K. Takayama, "Vorticity production in shock diffraction," *J. Fluid Mech.* **478**, 237–256 (2003).
- 8 P. Halder, S. De, K. Sinhamahapatra, and N. Singh, "Numerical simulation of shock-vortex interaction in Schardin's problem," *Shock Waves* **23**, 495–504 (2013).
- 9 R. Ripley, F.-S. Lien, and M. Yovanovich, "Numerical simulation of shock diffraction on unstructured meshes," *Comput. Fluids* **35**, 1420–1431 (2006).

- ¹⁰G. Abate and W. Shyy, "Dynamic structure of confined shocks undergoing sudden expansion," *Prog. Aerosp. Sci.* **38**, 23–42 (2002).
- ¹¹A. Chaudhuri, A. Hadjadj, O. Sadot, and G. Ben-Dor, "Numerical study of shock-wave mitigation through matrices of solid obstacles," *Shock Waves* **23**, 91–101 (2013).
- ¹²A. Chaudhuri, A. Hadjadj, O. Sadot, and E. Glazer, "Computational study of shock-wave interaction with solid obstacles using immersed boundary methods," *Int. J. Numer. Methods Eng.* **89**, 975–990 (2012).
- ¹³A. Chaudhuri, A. Hadjadj, O. Sadot, and G. Ben-Dor, "Study of shock-wave mitigation through solid obstacles," in *28th International Symposium on Shock Waves*, edited by K. Kontis (Springer Berlin Heidelberg, Berlin, Heidelberg, 2012), pp. 493–498.
- ¹⁴A. Chaudhuri, A. Hadjadj, and A. Chinnayya, "On the use of immersed boundary methods for shock/obstacle interactions," *J. Comput. Phys.* **230**, 1731–1748 (2011).
- ¹⁵E. Glazer, O. Sadot, A. Hadjadj, and A. Chaudhuri, "Velocity scaling of a shock wave reflected off a circular cylinder," *Phys. Rev. E* **83**, 066317 (2011).
- ¹⁶M. Shadloo, A. Hadjadj, and A. Chaudhuri, "On the onset of postshock flow instabilities over concave surfaces," *Phys. Fluids* **26**, 076101 (2014).
- ¹⁷V. Soni, A. Hadjadj, A. Chaudhuri, and G. Ben-Dor, "Shock-wave reflections over double-concave cylindrical reflectors," *J. Fluid Mech.* **813**, 70–84 (2017).
- ¹⁸A. Chaudhuri, G. Jacobs, W. Don, H. Abbassi, and F. Mashayek, "Explicit discontinuous spectral element method with entropy generation based artificial viscosity for shocked viscous flows," *J. Comput. Phys.* **332**, 99–117 (2017).
- ¹⁹A. Chaudhuri and G. B. Jacobs, "Dynamics of shock wave diffraction over sharp splitter geometry using entropy-based artificial viscosity method," *Shock Waves* **29**, 101–115 (2019).
- ²⁰A. Chaudhuri, "Shock propagation and diffraction through cavity," in *Proceedings of the 59th Conference on Simulation and Modelling (SIMS 59)*, 26–28 September 2018, Oslo Metropolitan University, Norway (Linköping University Electronic Press, Linköpings Universitet, 2018), Vol. 153, pp. 111–117.
- ²¹J. O. Reeves and B. Skews, "Unsteady three-dimensional compressible vortex flows generated during shock wave diffraction," *Shock Waves* **22**, 161–172 (2012).
- ²²S. Cooppan and B. Skews, "Three-dimensional shock wave diffraction off a discontinuous edge," *Shock Waves* **27**, 131–142 (2017).
- ²³B. W. Skews and J. J. Bentley, "Merging of two independent diffracting shock waves," *Shock Waves* **26**, 327–331 (2016).
- ²⁴K. Takayama and O. Inoue, "Shock wave diffraction over a 90 degree sharp corner—posters presented at 18th ISSW," *Shock Waves* **1**, 301–312 (1991).
- ²⁵B. Skews, C. Law, A. Muritala, and S. Bode, "Shear layer behavior resulting from shock wave diffraction," *Exp. Fluids* **52**, 417–424 (2012).
- ²⁶C. Law, A. Muritala, and B. Skews, "Unsteady flow with separation behind a shock wave diffracting over curved walls," *Shock Waves* **24**, 283–294 (2014).
- ²⁷A. Chaudhuri and A. Hadjadj, "Numerical investigations of transient nozzle flow separation," *Aerosp. Sci. Technol.* **53**, 10–21 (2016).
- ²⁸O. Ben-Nasr, A. Hadjadj, A. Chaudhuri, and M. S. Shadloo, "Assessment of subgrid-scale modeling for large-eddy simulation of a spatially-evolving compressible turbulent boundary layer," *Comput. Fluids* **151**, 144–158 (2017).
- ²⁹V. Soni, A. Hadjadj, and O. Roussel, "On the use of adaptive multiresolution method with time-varying tolerance for compressible fluid flows," *Shock Waves* **29**, 37–50 (2019).
- ³⁰B. W. Skews, "The shape of a diffracting shock wave," *J. Fluid Mech.* **29**, 297–304 (1967).
- ³¹C. B. da Silva and J. C. F. Pereira, "Invariants of the velocity-gradient, rate-of-strain, and rate-of-rotation tensors across the turbulent/nonturbulent interface in jets," *Phys. Fluids* **20**, 055101 (2008).
- ³²M. Gampert, J. Boschung, F. Hennig, M. Gauding, and N. Peters, "The vorticity versus the scalar criterion for the detection of the turbulent/non-turbulent interface," *J. Fluid Mech.* **750**, 578–596 (2014).
- ³³T. Watanabe, Y. Sakai, K. Nagata, Y. Ito, and T. Hayase, "Turbulent mixing of passive scalar near turbulent and non-turbulent interface in mixing layers," *Phys. Fluids* **27**, 085109 (2015).
- ³⁴R. Jahanbakhshi, N. S. Vaghefi, and C. K. Madnia, "Baroclinic vorticity generation near the turbulent/non-turbulent interface in a compressible shear layer," *Phys. Fluids* **27**, 105105 (2015).
- ³⁵G. Borrell and J. Jiménez, "Properties of the turbulent/non-turbulent interface in boundary layers," *J. Fluid Mech.* **801**, 554–596 (2016).
- ³⁶R. Jahanbakhshi and C. K. Madnia, "Entrainment in a compressible turbulent shear layer," *J. Fluid Mech.* **797**, 564–603 (2016).
- ³⁷P. Davidson, *Turbulence: An Introduction for Scientists and Engineers* (Oxford University Press, 2015).
- ³⁸A. Chaudhuri, A. Hadjadj, A. Chinnayya, and S. Palerm, "Numerical study of compressible mixing layers using high-order WENO schemes," *J. Sci. Comput.* **47**, 170–197 (2011).
- ³⁹L. Davidson, "Transport equations in incompressible URANS and LES," in Publication 2006/01, Chalmers University of Technology, 2006.
- ⁴⁰M. S. Chong, A. E. Perry, and B. J. Cantwell, "A general classification of three-dimensional flow fields," *Phys. Fluids A* **2**, 765–777 (1990).
- ⁴¹S. Pirozzoli and F. Grasso, "Direct numerical simulations of isotropic compressible turbulence: Influence of compressibility on dynamics and structures," *Phys. Fluids* **16**, 4386–4407 (2004).
- ⁴²N. S. Vaghefi and C. K. Madnia, "Local flow topology and velocity gradient invariants in compressible turbulent mixing layer," *J. Fluid Mech.* **774**, 67–94 (2015).
- ⁴³J. Wang, Y. Shi, L.-P. Wang, Z. Xiao, X. T. He, and S. Chen, "Effect of compressibility on the small-scale structures in isotropic turbulence," *J. Fluid Mech.* **713**, 588–631 (2012).
- ⁴⁴S. Suman and S. S. Girimaji, "Velocity gradient invariants and local flow-field topology in compressible turbulence," *J. Turbul.* **11**, N2 (2010).
- ⁴⁵K. Kumari, S. Mahapatra, S. Ghosh, and J. Mathew, "Invariants of velocity gradient tensor in supersonic turbulent pipe, nozzle, and diffuser flows," *Phys. Fluids* **30**, 015104 (2018).
- ⁴⁶J. Gaviglio, J. Dussauge, J. Debieve, and A. Favre, "Behavior of a turbulent flow, strongly out of equilibrium, at supersonic speeds," *Phys. Fluids* **20**, S179–S192 (1977).
- ⁴⁷J. P. Dussauge, J. Gaviglio, and A. Favre, "Density changes and turbulence production in the expansion or compression of a turbulent flow at supersonic speed," in *Structure and Mechanisms of Turbulence II*, edited by H. Fiedler (Springer Berlin Heidelberg, Berlin, Heidelberg, 1978), pp. 385–395.
- ⁴⁸G.-H. Cottet, D. Jiroveanu, and B. Michaux, "Vorticity dynamics and turbulence models for large-eddy simulations," *ESAIM: Math. Modell. Numer. Anal.* **37**, 187–207 (2003).